

In-situ Piezoresponse Force Microscopy Cantilever Shape Profiling

R. Proksch¹

Asylum Research, an Oxford Instruments Company, Santa Barbara, CA USA

The frequency dependent amplitude and phase shown in many Piezoresponse Force Microscopy (PFM) measurements are shown to be a consequence of the extended nature of Atomic Force Microscope (AFM) cantilever beams used to make the measurements. Changes in the cantilever shape as a function of changes in the boundary conditions (forces and frequencies) are the ultimate source of the sensitivity of cantilevers to forces between the tip and the sample. Because conventional PFM and AFM measurements are made with the motion of the cantilever measured at one optical beam location (typically near the end of the cantilever), the choice of this location will by necessity provide a limited picture of the total cantilever motion. In this work, the frequency dependence of PFM is in part explained in part by experimental measurements of the shape of the oscillating cantilever beam. This choice of spot location, typically at the end of the cantilever can lead to strong variations in the response of the lever stemming from changes in the cantilever sensor rather than from the response of the sample. It is well known that long-ranged electrostatics, since they can lead to a response at the drive frequency, contribute to the measured PFM signal. The significance of the electrostatics versus the piezoresponse depends on the optical detector Spot location on the cantilever. In particular, the optical sensitivity and the phase of the response is frequency dependent. Sample stiffness also contributes to complications and in some cases, in addition to conventional piezo-electromechanical effects causing hysteresis in the amplitude and phase observables, hysteresis in these observables can also stem from changes in the tip-sample stiffness, such as we might expect from localized electrochemical reactions.

¹ roger.proksch@oxinst.com

Coupling between electrical and mechanical phenomena is a common characteristic of many natural systems, with examples ranging from piezoelectric and ferroelectric,^{1, 2, 3, 4, 5} and energy storage materials^{6, 7, 8} to biological samples^{9, 10} ranging from molecules to complex tissues.¹¹ Based on the Atomic Force Microscope (AFM),¹² Piezoresponse Force Microscopy (PFM)^{13, 14} has become an established, powerful tool for functional nanoscale imaging, spectroscopy, and manipulation of ferroelectric and piezoelectric materials.

PFM is based on the converse piezoelectric effect, with the cantilever in contact mode while the tip-sample voltage is modulated with a periodic tip bias, $V_{\text{tip}} = V_{\text{dc}} + V_{\text{ac}} \cos(\omega t)$. This generates an oscillating electric field below the tip that causes localized deformations in the sample surface, which in turn act as a mechanical drive for the cantilever. The piezoelectric response of the surface is detected as the first harmonic component, $A_1\omega$, of the tip deflection, $A = A_0 + A_1\omega \cos(\omega t + \phi)$. When the response is dominated by the piezoelectric contribution, the phase of the electromechanical response of the surface, ϕ is dependent on the polarization direction. There are other forces present that respond at this harmonic – specifically localized electrostatic forces between the tip and sample surface charge and delocalized electrostatic forces between the body of the cantilever and the sample surface charge. In general, the larger the piezo response amplitude is relative to the other contributions improves the PFM contrast and allows more quantitative interpretation of the data.^{15, 16} Over the past years, a number of approaches for maximizing the PFM response and minimizing or eliminating the electrostatic components have been developed,^{17, 18} however, it remains a significant challenge.

Typically by using a lockin amplifier or band excitation¹⁹ (BE) techniques, the amplitude and phase of these electromechanical vibrations at the first drive harmonic are extracted and provide information on the piezoelectric orientation and strength of the material in the vicinity of the tip. Explicitly, the amplitude is related to the functional sensitivity of the material and the phase is related to the domain orientation. In addition to PFM, the recently developed Electrochemical Strain Microscopy (ESM)^{20, 21} technique relies on a oscillating tip-sample bias inducing localized ionic motion that in turn causes a strain that is coupled to the cantilever through the sharp tip.

One of the ongoing challenges of PFM, ESM and related techniques is the accurate characterization of functional parameters. The most common example of this is the inverse piezo sensitivity, a measure of the strain response of a piezo-electric material to an applied voltage, typically quoted in units of nm/V. Issues with accurate measurement of this parameter include (i) the tensorial nature of electromechanical coupling, (ii) uncertainties in the tip-sample mechanical interface, (iii) uncertainties in the calibration of the mechanical and sensorial properties of the cantilever and (iv) electrostatic forces between the body and tip of the cantilever competing with the piezo electric actuation.²²

Following Jesse et al.,²³ it is common to define an “effective” sensitivity $\tilde{d}_{\text{eff}} = A_z/V$ that combines the components of the piezoelectric tensor to describe the resulting response of the PFM cantilever to the applied voltage along the z-axis.^{24, 25, 26} The response of the cantilever at the first harmonic of the AC drive voltage is given by a combination of localized piezoresponse, localized electrostatic (capacitive) response and long range electrostatics between the sample and the cantilever body. There are similar relationships for lateral components, however here we will only consider the vertical PFM response. The capacitive coupling is generally responsible for a background signal at the drive frequency that complicates interpretation of the PFM response.^{27, 28} “Ideal” PFM measurements of ferroelectric materials follows some simple trends¹

1. Frequency-independent, at least below the first contact resonance frequency.
2. The amplitude should be independent of the ferroelectric polarization direction.²⁹
3. The phase shift across oppositely polarized domains should be 180°.

To elaborate on point #1 above, the mechanical resonances of bulk ferroelectric crystals are cases are well above the 1kHz - 1MHz PFM range.³⁰ However, it is well-known that the drive frequency of the electrical excitation can have a profound effect on the measured piezoresponse signal,^{31, 32} with at least part of the frequency dependence to the contact resonance of the cantilever.³³ Since the contact resonance depends on the contact stiffness of the tip-sample interaction, as the contact area changes while the cantilever scans over the surface, operating too close to the cantilever resonance can lead to artifacts in the response. Harnagea et al. suggested operating the contact cantilever near, but not exactly on a resonant frequency to enhance the response and at the same time avoid artifacts associated with changes in the contact resonance due to adhesion effects.³⁴

In addition to capacitive coupling, there are other sources of background that can cause crosstalk in the PFM response. (i) Instrumental resonances and/or electrical that cause a background in the PFM signal. The dangers of exciting instrumental electrical or mechanical resonances in the AFM while making PFM measurements have been elaborated.^{35, 36} In the Cypher AFM instrument used here, these effects have been effectively eliminated through careful design of the electrical signal routing and shielding.

In most cases, single frequency PFM has been limited to a few hundred kHz or lower³⁷ with some exceptions.^{38, 39} There are potential advantages to operation at higher frequencies including reduced sensitivity to electrostatic background contributions to the response and the dynamic stiffening of the lever at higher resonant modes. However, there are also complications associated with operating near resonance since it is well established that local elastic and contact area variations due to topography will also change the resonance frequency and thereby lead to crosstalk.⁴⁰ This effect has been largely mitigated through the use of resonance tracking techniques such as Dual AC Resonance Tracking (DART)⁴¹ and BE approaches. Both of these techniques allow the determination of the driving force or strain in PFM by properly accounting for shifting resonance and quality factor as the cantilever scans over the surface. It should also be noted that higher frequency operation in fluid is particularly useful since it avoids the electrolytic effects of low frequency biases. In some case, by operating at a high enough frequency, unshielded electrical probes can be used without inducing electrochemical interactions.⁴²

Cantilevers used in AFM applications are elastic beams that appear in a variety of shapes and sizes. The resonance frequency shift in response to tip-sample interactions is a strong function of the cantilever geometry.⁴³ Because they more closely obey analytic expressions, simple, diving board plan geometries are best suited for quantitative measurements. However, there can be substantial variations in cantilever shape due to mask mis-alignment, defects in the cantilever material and uncontrolled variations in production parameters. Thus, it is typical to see a wide range of cantilever parameters in micromachined cantilevers, with spring constants varying by as much as an order of magnitude.⁴⁴

As a convenient reference sample for this work, we chose a commonly available periodically poled LiNbO₃ (PPLN) sample.⁴⁵ LiNbO₃ belongs to point group 3m and therefore the piezoelectric matrix has four independent components: d_{15} , d_{22} , d_{31} , and d_{33} .⁴⁶ The vertical PFM signal far away from domain wall contains contributions from all of the components as described by Lei et al.,⁴⁷ but is dominated by the d_{33} and d_{15} contributions.

An example of frequency dependent PFM is shown in Figure 1. Figures 1(a)-(f) show the PFM phase for 10um scans on a periodically poled LiNiO₃ sample with the optical spot positioned at the tip of the cantilever. Histograms of the measured phase (data not shown) exhibit the expected 180 degree phase shift across oppositely poled domains with the exception of (b) and (e) where the low amplitude over the “up” domain leads to large phase fluctuations in the measured response. For the data in this

Figure, the tip-sample potential was oscillated at 40, 150, 190, 220, 310 and 330 kHz respectively. The last two frequencies were chosen to be just below and just above the contact resonance at ~ 320 kHz. The optical spot was positioned at the tip as is typical for maximizing the sensitivity of AFM measurements. The phase data generally show the expected 180 degree shifts over the two domains with the notable exceptions of 1(b), (c) and (d) where the phase goes through a noisy reversal, inverting between 1(b) and (d). The noisy phase images correspond to small amplitude regions in images (b') and (d'). Note that the drive voltage amplitude was held constant at $V_d = 3V$ during all of the measurements; so clearly, the application of $\tilde{d}_{eff} = A_z/V_d$ will lead to very different estimates of \tilde{d}_{33} . Perhaps even more clearly, the amplitude over the central “down” stripe domain is different from the “up” domain appearing larger at low frequencies (see Figure 1(a') and (b')) and smaller at high frequencies (see Figure 1(c')-(f')).

The amplitude asymmetries are in contrast to the “ideal” expectations discussed above. In one previous study, asymmetries were attributed to non-stoichiometric LiNbO_3 .⁴⁸ Electrostatic interactions between the cantilever and the surface are another source of asymmetries in the amplitudes. As is discussed below, these sorts of long-range interactions can have significant and measureable effects on the cantilever mode shape and may explain asymmetries in the amplitude response.⁴⁹ The RH for these experiments varied between 45-55%, leading us to expect several water layers and perhaps even a meniscus between the tip and the sample.⁵⁰ Water can affect charge injection and in similar samples we have observed inverse polarization effects.^{51, 52} Charge injection can lead to electrostatic forces between the tip and/or the body of the cantilever and the sample.

Figure 2(a) shows the phase spectra over the two domains at the red and black locations indicated in Figure 1(a) while Figure 2(b) shows the associated amplitude spectra. As with the data of Figure 1, these tunes were made with the optical spot positioned at the tip of the cantilever. The frequencies used in the six images of Figure 1 are labeled as dashed vertical blue lines. Note that the “noisy” phase signals, where the measured phase switches by 180 degrees (150 kHz for black and 220 kHz for red) correspond to a minima in the “Up” domain amplitude spectra in Figure 2(b). The 180 degree phase shift at the resonance frequency is a consequence of phase wrapping in the AFM lock-in amplifier. The amplitude axis is logarithmic, making the amplitude clearly visible at all frequencies despite the high quality factor ($Q \sim 100$) of the contact resonance. Inspection of the frequency response of at the four values indicated with the dashed blue lines shows they are consistent with the six images of Figure 1. One feature of note in both the Up and Down domain curves is the existence of a minimum in the amplitude curve, near 155 kHz for the Up domain and near 225 kHz for the Down domain. In both cases, there is a phase shift going through the minima frequency – despite being well below the contact resonance.

Ernst Chladni is credited with mapping the modal shapes of plates in response to different boundary conditions.⁵³ This same change of cantilever shape in response to changes in the boundary conditions is the fundamental basis for all AFM measurements. In many measurement modes, the changes are small, amounting to small perturbations of the shape that result in small but measureable changes in observables such as the resonance frequency, amplitude or phase. In other techniques, such as contact resonance as theoretically predicted by Rabe et al.,⁴³ the mode shape can experience radical changes. As part of their work, Rabe et al. mapped the mode shapes of a variety of **freely** vibrating rectangular levers using an optical interferometer. They found that the rectangular levers exhibited a good agreement with cantilever beam theory, though they did observe coupling between transverse and torsional modes. This initial work did not explore mode shapes of the cantilever interacting with the surface. Contact resonance measurements Since that pioneering work, there have been a number of other studies of the variation in the dynamic mode shape of vibrating cantilevers.^{54, 55, 56} In addition to these imaging applications, mode shape measurements have been useful for cantilever based sensing.^{57, 58, 59}

To study the effects of these drive mechanisms on the cantilever during PFM measurements, the response of the as a function of both frequency and optical beam spot position has been measured in-situ while the cantilever is probing a functional material. Figure 3 shows a schematic diagram of the setup used to scan the spot location over the cantilever while the lever is in contact with the surface as described by the six steps below.⁶⁰ We used the built-in motorized stage in a Cypher AFM to measure the cantilever deflection, amplitude and phase as a function of spot location. The lateral positioning precision of 200nm and the vertical precision of 40nm allows us to measure the response with great repeatability. The basic algorithm for making these measurements is as follows:

1. Establish the cantilever in a measurement mode. This could be a simple tune away from the surface, contact mode, tapping or as the case for this report, PFM mode.
2. At a single x y point on the surface, with the z-feedback loop operating allow the z-position to stabilize. If the z-position is drifting in time, this drift can be measured and used to extrapolate the control voltage when the z-feedback is disabled in the next step.
3. After stabilization or enough measurements to insure good extrapolation of the z-drift, disable the z-feedback. This is most easily accomplished by ramping the feedback gains to zero.
4. Reposition the spot at various points on the cantilever while recording the optical signal (deflection, amplitude and phase) as schematically illustrated in Figure 2(g).
5. Sweep the drive frequency (tip voltage in the case of PFM) to record the amplitude and phase as a function of both position and frequency.
6. Return the spot to the original position and ramp the feedback gains to the original values.

While doing this, the z-position as it responds to the feedback loop can be recorded to evaluate the effects of drift during the measurement steps 4-5. If there was significant drift, it is advisable to discard the measurements.

An example of an amplitude spectrogram obtained in this manner is shown in Figures 4(a) and 4(a') show the phase spectrograms and 4(b) and 4(b') show the corresponding amplitude spectrograms. The amplitudes were plotted using a logarithmic grayscale. The most notable feature of these results are the different nodal lines, visible as a swath of low amplitude points in the amplitude images and as a 180 degree phase shift in 3(b) and (c). The blue dotted lines in Figures 3(b) and (c) are to guide the eye. One unexpected result is that the nodal line – where the amplitude of the cantilever is ~ 0 and the measured phase goes through a 180 shift – is different for the two domains below resonance.

As is clear from the phase spectrograms of the Down domain (Figures 4(a) and (b)) and the Up domain (Figures 4(a') and (b')), the crossover between the dc response and first contact mode is measurable at surprisingly low frequencies. For the Down domain, the crossover is on the order of half the contact resonance frequency. For the Down domain, the crossover is even lower – nearly to DC. The dashed red lines in Figures 4(a) and (a') were sketched along the phase boundary. The overlap where there is very little phase contrast is shown as a blue-shaded region in Figure 4(c). It is also in the middle of what has been conventionally recommended as the best operating region for PFM. Specifically, (i) at a frequency well below the contact resonance³⁴ and (ii) with the optical spot positioned close to the end of the lever.

In single point-mass models of the cantilever, while long range electrostatic interactions are considered, they do not explain the behavior shown in Figures 2 and 3. Since the cantilever shape is changing, the measured amplitude and phase at a given spot position will also change. To account for this, it is necessary to go beyond the point-mass model discussed above and consider the extended cantilever beam shape.

After separating out the time dependence, the Euler-Bernoulli cantilever beam equation is given by

$$\frac{\partial^4 w(x)}{\partial x^4} - \beta^4 w(x) = \frac{3F_{elec}L}{k_{cant}}, \quad (1)$$

where $\beta = C_1 \sqrt{\frac{\omega}{\omega_0}}$. The extended electrostatic force F_{elec} , acts along the length of the cantilever

and has been extensively discussed as a complication in interpreting PFM response.^{61, 62, 63, 64, 65} Note that this term is divided by the stiffness of the cantilever, suggesting that the effect of long-ranged electrostatics can be reduced by choosing as stiff a cantilever as possible for a given measurement. This stiffness of course has practical limitations since large loading forces can damage tip coatings, the tip structure itself and the sample. Localized electrostatic and localized electromechanical responses are included through appropriate boundary conditions. On the clamped end of the cantilever, the displacement and deflection angle are zero; $w(0) = 0$ and $w'(0) = 0$. On the tip end, since we are neglecting any lateral component in the tip-sample interactions, $w''(L) = 0$. Localized forces, including both localized electrostatic interactions between the tip and sample along with piezoelectric strain forces couple lead to the shear force boundary condition $w'''(L) = \frac{k_{ts}}{EI}(w(L) - z_{em})$, where the

electromechanical strain is given by $z_{em} = d_{eff}V_d$. The excellent agreement between the experimental and theoretical spectrograms below resonance shown in Figures 4 and 5 justified omitting additional terms in the model such as the capacitive coupling between the tip and sample, the sample work function, the electrical contact quality or position-sensitive contact stiffness across the two domains. Equation (1) was solved analytically using Mathematica and then used to compute theoretical spectrograms shown in Figures 4(d), 4(d') and 5(a')-(c'). Note that the theoretical spectrograms were of the derivative of the height function to match the slope detection response of the optical lever detector.⁶⁰ The sub-resonance asymmetric nodal lines visible in Figures 4(b) and (b') are easily duplicated with this model as shown in Figures 4(d) and (d') respectively. This asymmetry is consistent with a background electrostatic force consistent with capacitive coupling between the body of the cantilever and the charged sample surface.⁴³

It should be noted that there were significant differences in the response near resonance in the two domains. In particular, the amplitude of the Up domain was smaller than the Down and It was possible to explain these differences with additional terms in the model above, specifically an additional tip-sample capacitance and domain specific damping. A detailed analysis of those effects is beyond the scope of this paper but is consistent with differences in surface contamination between the two domains.

The model calculations can also be used to compare spectrograms made at applied DC bias voltages. The electrostatic coupling between the body of the cantilever and the sample surface was estimated by positioning the cantilever ~100nm above the surface (out of contact) and then measuring the bias-dependent electromechanical response. This allowed the non-localized F_{elec} to be characterized for subsequent contact measurements (see supplemental materials). This is admittedly slightly different conditions than those in the contact profiles but the voltage agreement between the experimental and theoretical measurements in Figure 5 justify this approach. Figure 5 shows bias dependent spectrograms measured over a domain made with +5, 0 and -5 volt dc biases applied to the tip. The bright vertical band in Figures 5(a-c) corresponds to an instrumental artifact and can be neglected. The bias-dependent evolution of the antinode positions (dark, low-amplitude regions) shown

in 5(a-c) in the experimental bands is strikingly reproduced by the theoretical calculations, $5(a'-c')$. The only adjustment used in these images was the bias-dependent strain at the tip, z_{em} , or equivalently, the piezo coupling coefficient, d_{eff} . A value of $d_{eff}=105\text{pm/V}$ used to generate the data of Figures 5(a'-c'). While this is not the expected value, it is within the range measured by others as discussed above.

These experiments were initially motivated by trying to improve the quantitative PFM measurements and the results indeed suggest some strategies for improving these measurements. Notably, of the two independent variables in the spectrograms, the response was most nearly ideal, with 180 degree phase shifts and equal amplitudes over opposite domains when the frequency was very low $<10\text{kHz}$. Near resonance, the phase contrast was well behaved but there were differences in the amplitudes of the responses. While these differences could be explained with a slightly more complicated model, it does imply that care needs to be taken with interpreting the response near resonance.^{66, 67} At the same time, the enhanced signal to noise provided by imaging at resonance provides a benefit that can be well worth this tradeoff.

These results also confirm many of the prior experimental conclusions for making quantitative PFM measurements. In the absence of making these sorts of careful position and frequency dependent measurements, quantitative measurements can be improved by minimizing the effects of long-range coupling between the cantilever:

1. Choosing a low drive frequency. While this was indeed confirmed, the definition of “low” depends very strongly on the electrostatic term and may in some cases be well below even a few kHz. Even 5-10kHz for the drive frequency may not be sufficient for quantitative PFM.
2. If operating on resonance, which is desirable for improved signal to noise, care must be taken in interpreting the response. Specifically, the effects of the
3. Smaller cantilevers to reduce the capacitive coupling between the tip and sample.
4. Longer tips to reduce the capacitance between the tip and sample.
5. Shielded probes may reduce the capacitance but are also more expensive and not as well-developed as conventional cantilevers at this point.
6. Stiffer cantilevers also will reduce the significance of the long-ranged electrostatic forces but may be undesirable for thin films and softer materials since the high loading force may damage the sample.
7. Scanning along the edge of a sample are also approaches that may help minimize these long range electrical effects.

Conclusions

We have developed a method for measuring the dynamic response of a cantilever to tip-sample interactions while cantilever is interacting with the sample. This technique can be applied to almost any AFM measurement modes, subject to the experimental constraints discussed above. We anticipate these constraints will ease as instrumentation evolves to even lower rates of thermal drift. In the case of PFM measurements, we presented maps of the cantilever modal response as a function of optical spot position and frequency through the first contact resonance.

The spatially extended response of a PFM cantilever has been shown to have excellent agreement with a relatively simple model that includes a piezoelectric drive centered at the tip and an extended electrostatic drive along the body of the cantilever. This pair of drive parameters enables excellent agreement between experimental and theoretical spectrograms. In the case where there are long range electrical interactions between the cantilever and the sample such as the case shown here, proper measurement of d_{33} depends on a choice of drive frequency and spot location. In particular, there

are some locations where small changes in the boundary conditions (such as tip-sample stiffness) or the balance of electrostatic versus piezoelectric forces can cause contrast inversions and amplitude changes that may be mistaken for polarization changes in the sample. Note that these effects can occur in zero DC applied bias. This also suggests that in the absence of making these sorts of careful position and frequency dependent measurements, the effects of long-range coupling between the cantilever should be minimized, perhaps with smaller cantilevers, longer tips, shielded probes, scanning along the edge of a sample or some combination of these approaches.

We anticipate that this approach to studying cantilever dynamics can be improved upon. One concern we have had is the potential presence of nonlinearities in the drive or detection method. An improvement we have started to explore is to operate in a constant amplitude mode where the drive amplitude is modulated as a function of frequency to maintain the resulting cantilever motion at the same amplitude. In contrast to earlier mode measurement approaches, these measurements are fully integrated into the AFM. In addition, since the sensor is the same, the optical lever sensitivity of the mode profile measurement exactly matches that of the AFM or PFM measurement. This can be run in any imaging mode including Contact, Contact resonance, PFM, Electrochemical Strain Microscopy, tapping, dual AC and force-distance measurements, both at high and low speed.

Figures

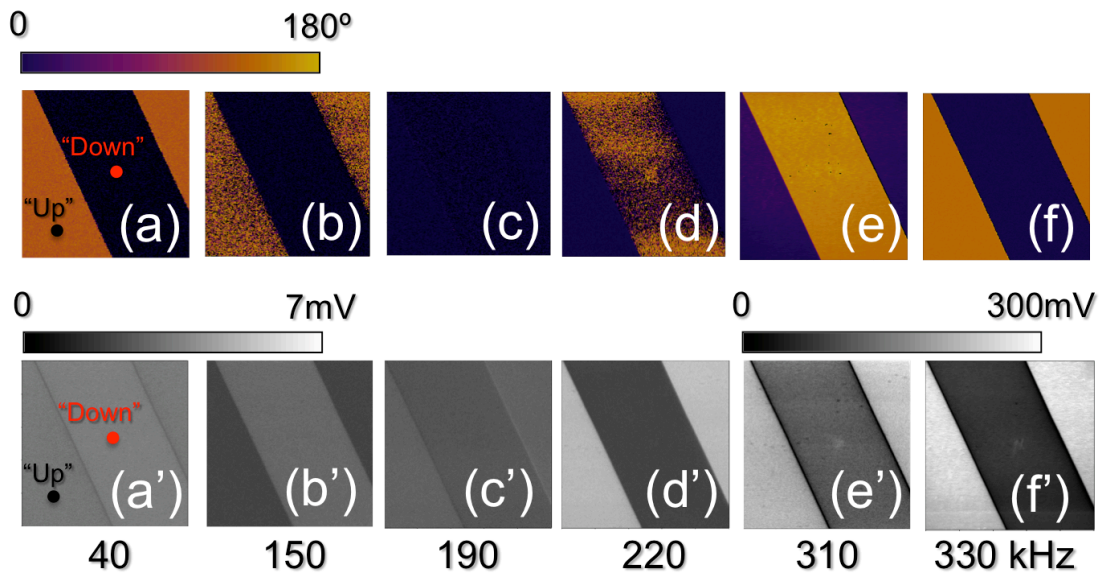


Figure 1 frequency-dependent PFM response on a periodically poled LiNbO₃ sample. The phase is shown in images (a)-(f) and the amplitude in images (a')-(f') for 40kHz, 150kHz, 190kHz, 220kHz and 330kHz respectively. The contact resonance was ~320kHz. The 7mV amplitude scale bar is for images (a')-(d') and the 300mV scale bar is for images (e') and (f').

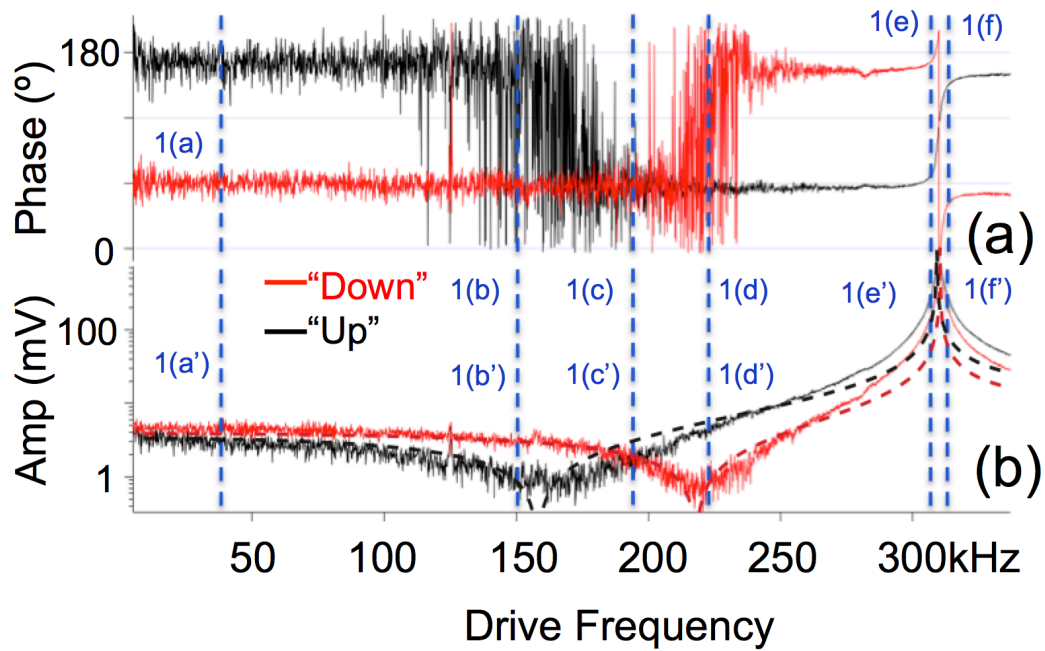


Figure 2(a) shows the phase spectra over the two domains at the red and black locations indicated in Figure 1(a) and 1(a'). Figure 2 (b) shows the associated amplitude spectra, plotted on a log scale. The labels (a)-(d) and (a')-(d') indicate the drive frequencies used to acquire the images shown in Figure 1. The dashed lines correspond to the modeled tunes discussed in the text and Figures 4 (c) and (c').

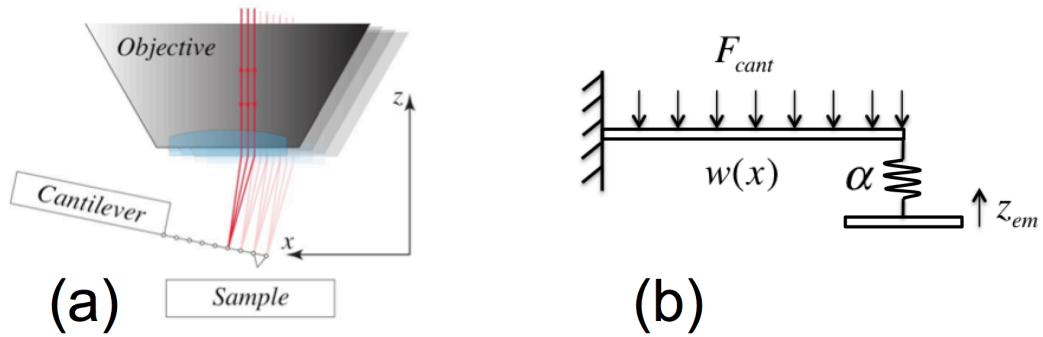


Figure 3 (b) Schematic of the motorized spot positioning system used to scan the optical spot along the length of the cantilever. The spot can be scanned in all three dimensions, insuring that it remains in-focus as it is scanned along the length of the tilted cantilever. (b)

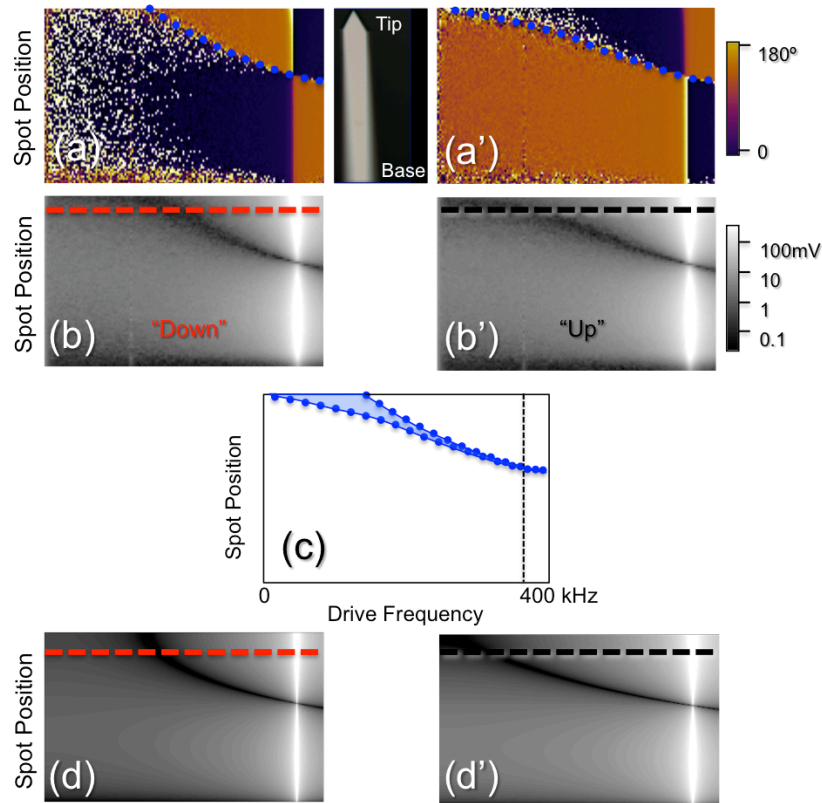


Figure 4 frequency-dependent and optical spot location dependent PFM response on a periodically poled LiNbO₃ sample. (a) and (b) and show the “down domain Phase and amplitude respectively while the “up” domain is phase and amplitude is shown in (a’) and (b’) respectively. The spectrograms show the phase and the logarithm of the amplitude as a function of frequency (0 to 350kHz) on the horizontal axis and spot position on the vertical, (base on the bottom, tip on the top). The dashed blue lines in (a) and (a’) show the locations of the amplitude antinodes – where the amplitude goes through a minima and the phase reverses. Figure (c) shows the “trouble zone” where the region with roughly zero phase contrast is

shaded in blue. This region happens to be in the range where many conventional sub-resonance PFM measurements take place, with the optical lever spot positioned near the tip of the cantilever and the drive frequency at a value substantially lower than resonance. Figure (d) shows the theoretically modeled amplitude spectrogram over the “down” domain while (d’) shows the theoretical amplitude for the “up” domain. Specific parameters to obtain these theoretical results are discussed in the text. The dashed lines in (b), (b’), (c) and (c’) are the tunes with the optical spot positioned near the end of the cantilever in Figure 2. (d)

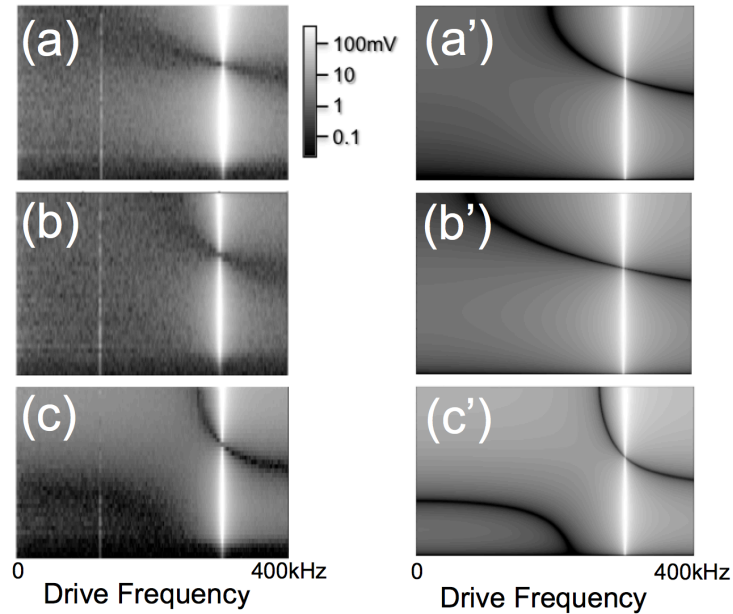


Figure 5 Experimental and theoretical bias voltage dependent spectrograms using an Asyelec lever over a LiNbO₃ domain. (a) +5V bias, (b) a 0 V bias and a (c) -5V bias. (a’), (b’) and (c’) show the simulated amplitude spectrograms for the respective bias voltages.

ACKNOWLEDGMENTS

The author thanks J. E. Sader for discussions and an introduction to beam theory within Mathematica™ during the early parts of this work. Ryan Wagner provided mathematical error checking and along with Arvind Raman, ongoing discussions and suggestions.

REFERENCES

- ¹ M. E. Lines and A. M. Glass, *Principles and Applications of Ferroelectrics and Related Materials*. Clarendon Press, Oxford, 1979.
- ² S. V. Kalinin, B. J. Rodriguez, J. D. Budai, S. Jesse, A. N. Morozovska, A. A. Bokov, and Z. G. Ye, *Phys. Rev. B* **81**, 064107 (2010).
- ³ V. Shvartsman and A. Kholkin, *J. Appl. Phys.* **101**, 064108 (2007).
- ⁴ V. Shvartsman, A. Kholkin, M. Tyunina, and J. Levoska, *Appl. Phys. Lett.* **86**, 222907 (2005).
- ⁵ A. Kholkin, A. Morozovska, D. Kiselev, I. Bdikin, B. Rodriguez, P. Wu, A. Bokov, Z. G. Ye, B. Dkhil, and L. Q. Chen, *Adv. Funct. Mater.* **21**, 1977 (2011).
- ⁶ Nazri, G. A.; Pistoia, G. *Lithium Batteries: Science and Technology*; Springer-Verlag: New York, 2009.
- ⁷ Abraham, K. M.; Jiang, Z. J. *Electrochem. Soc.* **143**, 1–5 (1996).
- ⁸ O'Hayre, R.; Cha, S. W.; Colella, W.; Prinz, F. B. *Fuel Cell Fundamentals*; John Wiley & Sons: New York, 2009.
- ⁹ S. V. Kalinin, B. J. Rodriguez, S. Jesse, T. Thundat and A. Gruverman, *Appl. Phys. Lett.* **87**, 053901 (2005).
- ¹⁰ S. V. Kalinin, E. Eliseev, A. Morozovska, *Appl. Phys. Lett.* **88**, 232904 (2006).
- ¹¹ Y. M. Liu, YJ Wang, M. J. Chow, N. Q. Chen, F. Ma, Y Zhang, and J. Li, *Phys. Rev. Lett.* **16** 168101 (2013).
- ¹² Binnig, Quate and Gerber, *Phys. Rev. Lett.* **56**, 930–933 (1986).
- ¹³ A. Gruverman and A. Kholkin, *Rep. Prog. Phys.* **69**, 2443 (2006).
- ¹⁴ S.V. Kalinin, A.N. Morozovska, L.Q. Chen, B.J. Rodriguez, *Rep. Prog. Phys.* **73**, 056502 (2010).
- ¹⁵ K. Franke, H. Huelz and M. Weihnacht *Surf. Sci.* **415** 178 (1998).
- ¹⁶ S. Hong, J. Woo, H. Shin, J. U. Jeon, Y. E. Park, E. Colla, N. Setter, E. Kim and K. No. *J. Appl. Phys.* **89** 1377 (2001).
- ¹⁷ C. Harnagea, M. Alexe, D. Hesse and A. Pignolet *Appl. Phys. Lett.* **83** 338 (2003).
- ¹⁸ B. D. Huey, C. Ramanujan, M. Bobji, J. Blendell, G. White, R. Szoszkiewicz and A. Kulik *J. Electroceram.* **13** 287 (2004).
- ¹⁹ S. Jesse, S. Kalinin, R. Proksch, A. P. Baddorf and B. Rodriguez, *Nanotechnology* **18** 435503 (2007).
- ²⁰ N. Balke, S. Jesse, A.N. Morozovska, E. Eliseev, D. W. Chung, Y. Kim, L. Adamczyk, R. E. Garcia, N. Dudney and S.V. Kalinin. *Nature Nanotech.* **5**, 749 (2010).

-
- ²¹ N. Balke, S. Jesse, Y. Kim, L. Adamczyk, A. Tselev, I.N. Ivanov, N.J. Dudney, and S.V. Kalinin, *Nano Lett.* **10**, 3420 (2010).
- ²² S. V. Kalinin, R. Shao, and D. A. Bonnell, *J. Am. Ceram. Soc.* **88**, 1077 (2005); S. Jesse, A. P. Baddorf, and S. V. Kalinin, *Nanotechnology* **17**, 1615 (2006).
- ²³ S Jesse, S Guo, A Kumar, B J Rodriguez, R Proksch and S V Kalinin, *Nanotechnology* **21** 405703 (2010).
- ²⁴ S. V. Kalinin, A. N. Morozovska, L. Q. Chen, and B. J. Rodriguez, *Rep. Prog. Phys.* **73**, 056502 (2010).
- ²⁵ N. Balke, I. Bdikin, S. V. Kalinin, and A. L. Kholkin, *J. Am. Ceram.Soc.* **92**, 1629 (2009).
- ²⁶ S. V. Kalinin, A. Rar, and S. Jesse, *IEEE Trans. Ultrason. Ferroelectr. Freq. Control* **53**, 2226 (2006).
- ²⁷ J. A. Christman, J. R. R. Woolcott, A. I. Kingon, and R. J. Nemanich, *Appl. Phys. Lett.* **73**, 3851 (1998).
- ²⁸ B. J. Rodriguez, S. Jesse. Seal, A. P. Baddorf, S. Habelitz and S. V. Kalinin, *Nanotechnology* **20** 195701 (2009).
- ²⁹ H.-N. Lin, S.-H. Chen, S.-T. Ho, P.-R. Chen, and I.-N. Lin *J. Vac. Sci. Technol. B* **21**, 916 (2003).
- ³⁰ J. W. Burgess, *J. Phys. D* **8**, 283 (1975).
- ³¹ C. Harnagea, A. Pignolet, M. Alexe, D. Hesse, and U. Gösele, *Appl. Phys. A: Mater. Sci. Process.* **70**, 1 (2000).
- ³² H. Bo et al., *J. Appl. Phys.* **108**, 042003 (2010).
- ³³ Jesse S, Mirman B and Kalinin S V *Appl. Phys. Lett.* **89** 022906 (2006).
- ³⁴ C. Harnagea, M. Alexe, D. Hesse and A. Pignolet, *Appl. Phys. Lett.* **83**, 338 (2003).
- ³⁵ T. Jungk, A. Hoffmann, and E. Soergel, *Appl. Phys. Lett.*, **89**, 163507 (2006).
- ³⁶ T. Jungk, A. Hoffmann, and E. Soergel, submitted (2007).
- ³⁷ I. K. Bdikin, V. V. Shvartsman, S. H. Kim, J. M. Herrero and A. L. Kholkin, *MATERIALS RESEARCH SOCIETY SYMPOSIUM PROCEEDINGS*, 784 83-88 (2004).
- ³⁸ B. D. Huey, in *Nanoscale Phenomena in Ferroelectric Thin Films*, edited by S. Hong Kluwer, New York, (2004).
- ³⁹ K. Seal, S. Jesse, B. J. Rodriguez, A. P. Baddorf and S. V. Kalinin, *Appl. Phys. Lett.* **91**, 232904 (2007).
- ⁴⁰ S Jesse, S Guo, A Kumar, B J Rodriguez2, R Proksch and S V Kalinin, *Nanotechnology* **21** 405703 (2010).
- ⁴¹ DART ref here

-
- ⁴² Mirman, B.; Kalinin, S. V. Resonance Frequency Analysis for Surface-Coupled Atomic Force Microscopy Cantilever in Ambient and Liquid Environments. *Appl. Phys. Lett.* 2008, 92, 083102
- ⁴³ U. Rabe, K. Janser, and W. Arnold, *Rev. Sci. Instrum.* 67 (9), 3281 (1996).
- ⁴⁴ Cantilever variations – Olympus, Nanosensors
- ⁴⁵ AR-PPLN LiNbO₃ test sample, Asylum Research, Santa Barbara, CA: <http://www.asylumresearch.com/Products/AR-PPLN/AR-PPLN.shtml>
- ⁴⁶ M. Jazbinsek and M. Zgonik, *Appl. Phys. B* 74, 407 (2002).
- ⁴⁷ S. Lei, E. A. Eliseev, A. N. Morozovska, R. C. Haislmaier, T. T. A. Lummen, W. Cao, S. V. Kalinin, and V. Gopalan, *Phys. Rev. B* 86 134115 (2012).
- ⁴⁸ D. A. Scrymgeour and V. Gopalan, *Phys. Rev. B* 72, 024103 (2005).
- ⁴⁹ S.V. Kalinin, D.A. Bonnell, *Nano Lett.* 4 555 (2004).
- ⁵⁰ B.L. Weeks, M.W. Vaughn, J.J. DeYoreo, *Langmuir*, 21 8096 (2005).
- ⁵¹ X. Sun, Y.J. Su, K.W. Gao, L.Q. Guo, L.J. Qiao, W.Y. Chu, *J Appl Phys*, 110 014103 (2011).
- ⁵² X. Sun, Y.J. Su, X. Li, K.W. Gao, L.J. Qiao, *J Appl Phys*. 111 094110 (2012).
- ⁵³ Ernst Chladni, *Entdeckungen über die Theorie des Klanges*, (1787).
- ⁵⁴ P. Vairac and B. Cretin, *Surf. Interface Anal.* 27, 588-591 (1999).
- ⁵⁵ Matthew S. Allen, Hartono Sumali and Peter C. Penegor, *Journal of Dynamic Systems, Measurement, and Control* 131 (2009).
- ⁵⁶ M. Spletzer, A. Raman and R. Reifenger, *J. Micromech. Microeng.* 20 085024 (2010).
- ⁵⁷ J. Mertens, M. Álvarez, and J. Tamayo, *Appl. Phys. Lett.* 87, 234102 (2005).
- ⁵⁸ P. Vairac and B. Cretin, *Surf. Interface Anal.* 27, 588-591 (1999).
- ⁵⁹ Matthew Spletzer, Arvind Raman and Ron Reifenger, *J. Micromech. Microeng.* 20 085024 (2010).
- ⁶⁰ Ryan Wagner, Arvind Raman and Roger Proksch, *Appl. Phys. Lett.* 103, 263102 (2013).
- ⁶¹ S. V. Kalinin, and D. A. Bonnell, *Phys. Rev. B* 63, 125411 (2001).
- ⁶² T. Hochwitz, A. K. Henning, C. Levey, C. Daghljan, and J. Slinkman, *J. Vac. Sci. Technol. B* 14, 457 (1996)

⁶³ S. Belaidi, P. Girard, and G. Leveque, J. Appl. Phys. **81**, 1023 (1997).

⁶⁴ S. Hong, J. Woo, H. Shin, J. U. Jeon, Y. E. Pak, E. L. Colla, N. Setter, E. Kim, and K. No, J. Appl. Phys. **89**, 1377 (2001).

⁶⁵ S. Hong et al., Appl. Phys. Lett. **80(8)** 1453 (2002).

⁶⁶ A Gannepalli, D G Yablon, A H Tsou and R Proksch, Nanotechnology 22 355705 (2011).

⁶⁷ Shuhong Xie et al., Nanoscale, **4**, 408 (2012).